EDGE ARTICLE

Check for updates

All publication charges for this article have been paid for by the Royal Society of Chemistry

Dipole-mediated interfacial solvation for efficient Li-ion transport in dendrite-free Li metal batteries

Wenlong Zhao,†[ab] Kui Xu,†[c] Yanyan Zhang, [ID] *[a] Qingyu Dong,[b] Ningyuan Zhang,[b] Huihui Wang,[b] Ruowei Yi,*[bd] Yuxin Tang, [ID] [a] Yanbin Shen [ID] *[b] and Liwei Chen[e]

Efficient Li$^+$ transport is crucial for ensuring the stability of Li metal anodes in Li metal batteries (LMBs). However, conventional vehicular transport in non-aqueous electrolytes, where Li$^+$ migrates with an intact solvation shell, results in sluggish ion transport kinetics, thereby exaggerating Li$^+$ flux heterogeneity and promoting dendritic deposition. Here, we propose a dipole-mediated solid–liquid interfacial solvation regulation strategy that leverages the abundant interface provided by a nano-ceramic electrolyte coating on the separator to accelerate and homogenize the Li$^+$ transport. The high-dipole molecule 2,5-difluoro-4-nitrobenzoic acid (DNA) was employed to functionalize the ceramic coating, inducing strong ion–dipole interactions with Li$^+$ and lowering the transport energy barrier at the interfacial region. Its low LUMO level further enables preferential reduction to generate a Li$_3$N/LiF-enriched interphase, stabilizing the Li surface and suppressing electrolyte decomposition. As a result, the dipole-regulated interface delivers a high ionic conductivity (0.517 mS cm^{-1}, compared with the pristine separator at 0.308 mS cm^{-1}) and a Li$^+$ transference number of 0.646, enabling dendrite-free Li deposition. Li‖LiFePO$_4$ and Li‖NMC811 full cells exhibit markedly improved long-term cycling stability under high areal-capacity loadings, demonstrating the effectiveness and practical viability of this dipole-mediated interfacial solvation strategy for enhancing ion transport in LMBs.

1 Introduction

Li metal batteries (LMBs) are among the most promising next-generation energy-storage systems owing to the ultrahigh theoretical capacity (3860 mAh g^{-1}) and the lowest redox potential (−3.04 V *vs.* SHE) of Li metal anodes.[1–3] Nevertheless, their practical deployment is severely hindered by uncontrolled dendritic formation and vigorous interfacial parasitic reactions, which together pose severe safety risks and limited cycle life.[4,5] Achieving a stable Li anode therefore requires precise regulation of Li deposition and robust interfacial stability. To mitigate these issues, various strategies have been explored, including electrolyte engineering (*e.g.*, functional additives,[6,7] high-concentration electrolytes[8,9]) and anode design (three-dimensional conductive frameworks,[10,11] artificial SEI

layers,[12–14] *in situ* Li-alloy anodes[15]). Moreover, the intrinsically uneven Li$^+$ flux arising from sluggish ion diffusion has been identified as a major contributor to non-uniform nucleation and dendritic propagation during Li plating/stripping.[16,17]

Separator functionalization has received extensive attention recently due to its crucial role in regulating Li$^+$ behavior and stabilizing electrode interfaces without altering the bulk electrolyte composition.[18,19] Among these approaches, coating polyolefin separators with ceramic solid-state electrolytes has attracted particular interest.[20–22] Such electrolyte layers improve thermal stability, mechanical robustness, and help construct more continuous Li$^+$ transport pathways, thereby homogenizing ionic flux at the separator/electrode interface.[23,24] The Li$^+$-transport mechanism in such ceramic frameworks typically involves site-to-site hopping through interconnected Li$^+$ migration channels (*e.g.*, M–O polyhedra in oxide ceramics), enabling steady-state conduction under a uniform electrochemical potential gradient.[25,26] However, in practical hybrid solid–liquid systems, Li$^+$ transport in the liquid phase still follows a solvent-coordinated vehicular mechanism, which is fundamentally different from mechanism.[27,28] This mismatch in transport modes leads to inhomogeneous ion flux and creates local transport bottlenecks, aggravating Li$^+$ depletion or accumulation regions and ultimately limiting deposition uniformity.[29,30] Therefore, further enhancing Li$^+$ transport efficiency

[a]*College of Chemical Engineering, Fuzhou University, Fuzhou 350002, China. E-mail: zyanyan@fzu.edu.cn*

[b]*i-Lab, Suzhou Institute of Nano-Tech and Nano-Bionics, Chinese Academy of Sciences, Suzhou 215123, China. E-mail: ybshen2017@sinano.ac.cn*

[c]*School of Flexible Electronics (Future Technologies), Institute of Advanced Materials, Nanjing Tech University, Nanjing, 211816, China*

[d]*School of Chemistry, Xiangtan University, Xiangtan 411105, China. E-mail: rwyi@xtu.edu.cn*

[e]*In Situ Center for Physical Sciences, School of Chemistry and Chemical Engineering, Shanghai Jiaotong University, Shanghai 200240, China*

† Both authors contributed equally to this work.

within hybrid solid–liquid systems is crucial for achieving high-performance LMBs.[31]

Bearing these considerations in mind, we focused on the rich solid–liquid interfaces in the system and proposed a dipole-mediated interfacial regulation strategy to tailor Li$^+$ solvation and enhance interfacial ion transport by introducing strongly polar molecules. By grafting a high-dipole modifier onto the nano-ceramic surface, the interfacial dipole field reorganizes the local Li$^+$ solvation structure and establishes accelerated migration pathways (Fig. 1a). The ion–dipole interaction energy can be described by the following equations:

$$U_{ion-dipole} = \frac{q\mu \cos \theta}{4\pi\varepsilon_0 r^2} \tag{1}$$

where U denotes the electrostatic energy, ε_0 is the dielectric constant, q represents the ionic charge, r is the ion–dipole distance, μ denotes the dipole moment of the solvent molecule, and θ is the angle between the ion direction and the dipole axis.[32,33] As the U is proportional to the dipole moment, a strong surface dipole modifier can reorganize Li$^+$ solvation and effectively lower the interfacial migration energy barrier, which can be quantitatively expressed as the vector sum of interfacial dipole–ion interaction forces (Fig. 1b). This dipole-mediated interfacial regulation bridges the transport-mode mismatch in hybrid systems and enables more uniform and efficient Li$^+$ flux, thereby promoting dendrite-free Li deposition.

Based on this concept, we employed the highly polar molecule 2,5-difluoro-4-nitrobenzoic acid (DNA) to functionalize the interface in a polypropylene (PP) separator coated with Li$_{1.4}$Al$_{0.2}$Ti$_{1.8}$Si$_{0.2}$P$_{2.8}$O$_{12}$ (LATSP) nanoparticles. The strong electron-withdrawing groups (–F, –NO$_2$) in DNA impart a large dipole moment, thereby inducing ion–dipole coupling that facilitate
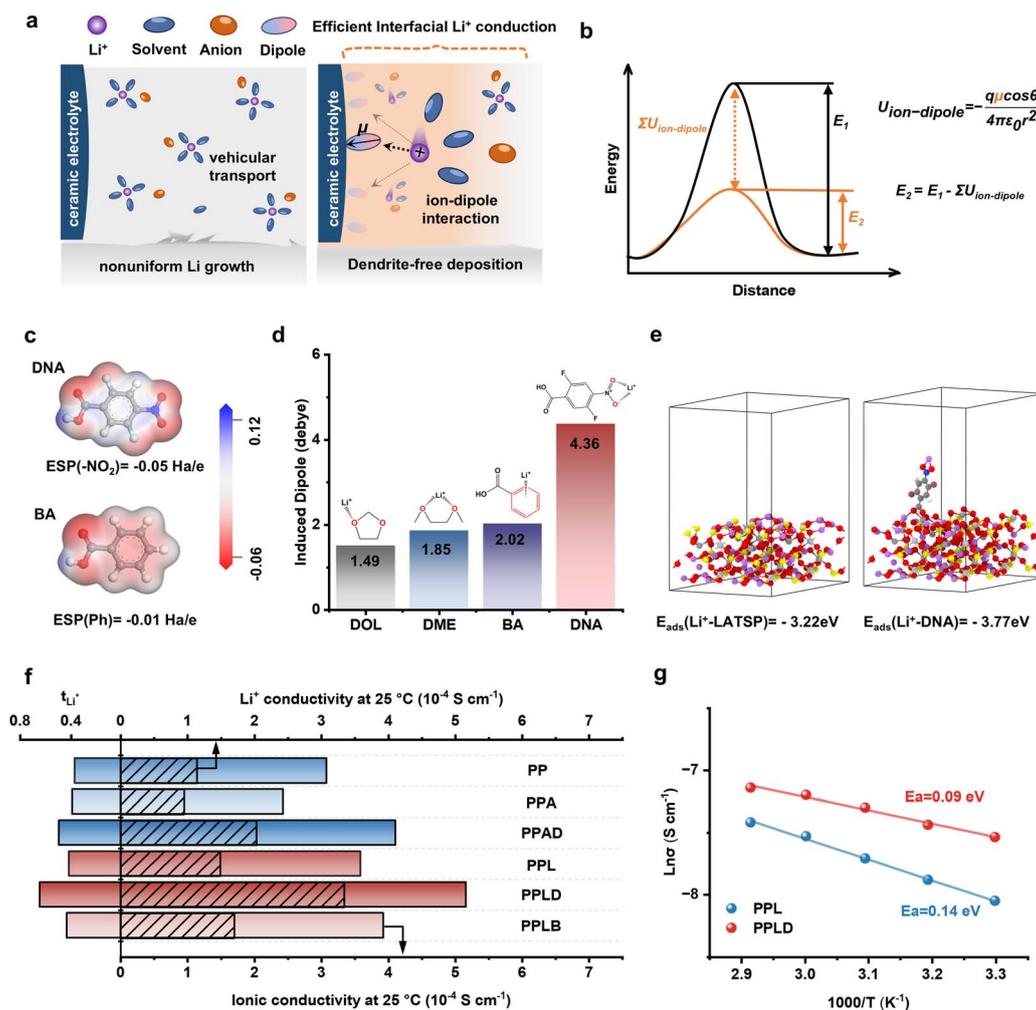

Fig. 1 (a) Schematic illustrating the accelerated Li$^+$ migration pathways at the solid–liquid interface enabled by dipole-mediated interfacial regulation. (b) Reduction of the Li$^+$ transport energy barrier via ion–dipole interactions. (c) Simulated ESP mapping of DNA and BA molecules. (d) Comparison of the induced dipole moments of DME, DOL, and DNA molecules coordinated with a single Li$^+$ ion. (e) The binding energy comparison between Li$^+$ adsorbed on the LATSP surface and at the –NO$_2$ site of the LATSP@DNA surface. (f) Comparison of ionic conductivity, Li$^+$ transference number, and Li$^+$ conductivity for different separators soaked in the ether-based electrolyte. (g) The Arrhenius fitting results and activation energies of PPL and PPLD separators soaked in the ether-based electrolyte. The plots are presented as ln(σ) versus 1000/T, where σ denotes the ionic conductivity.

efficient Li$^+$ migration at the LATSP/electrolyte interface and improving interfacial Li$^+$ transport kinetics. Moreover, its low LUMO level enables preferential reduction upon contact with Li metal, forming a Li$_3$N/LiF-rich interphase, that suppresses excessive electrolyte decomposition, prevents reductive degradation of LATSP, and enhances interfacial kinetic stability. This synergistic effect accelerates Li$^+$ transport and stabilizes the Li metal interface, leading to a high ionic conductivity of 0.517 mS cm^{-1} and a Li$^+$ transference number of 0.646 in an ether-based mixture system. As a result, Li‖LiFePO$_4$ cells exhibit stable cycling for 700 cycles at 1C, and Li‖NMC811 pouch cells with a high cathode loading (20 mg cm^{-2}) retain 88.29% of initial capacity after 230 cycles at 0.2C. This work demonstrates a practical molecular-level interfacial-engineering strategy for enabling efficient Li$^+$ transport in stable Li metal batteries.

2 Results and discussion

2.1 Theoretical calculation and interfacial ion transport mechanism exploration

To clarify the promoting effect of DNA on Li$^+$ transport and migration, theoretical calculations combined with interfacial ion-transport analyses were performed. Electrostatic potential (ESP) simulations further confirm the strong polarity of DNA. For further clarification, benzoic acid (BA) molecule without –NO$_2$ and –F groups was also studied. As shown in Fig. 1c, DNA exhibits a significantly more asymmetric charge distribution than the weakly polar BA, which arises primarily from the –NO$_2$ and –F substituents. This is quantitatively reflected in their dipole moments: DNA has a dipole moment of 3.43 D, whereas BA only exhibits 2.21 D, highlighting the much stronger polarity of DNA (Fig. S1).

The highly polarized electron distribution of DNA enables a much stronger Li$^+$–dipole interaction than that of BA or conventional ether solvents. This effect is quantitatively reflected in the density functional theory (DFT)-calculated induced dipole moments of Li$^+$-coordinated molecules (Fig. 1d). Upon binding with a single Li$^+$, 1,3-dioxolane (DOL), 1,2-dimethoxyethane (DME) and BA exhibit induced dipole moments of 1.49, 1.85, and 2.02 debye, respectively, whereas DNA reaches a significantly larger value of 4.36 debye. These results indicate that DNA can effectively dominate the interfacial solvation environment, partially replacing solvent molecules in the primary solvation shell and facilitating fast Li$^+$ transport at the LATSP surface. DFT calculations further reveal the energetic preference for Li$^+$ adsorption on the LATSP@DNA interface. Compared with Li$^+$ binding on the pristine LATSP surface (−3.22 eV), Li$^+$ coordination to the –NO$_2$ group of DNA exhibits a significantly more negative binding energy (−3.77 eV) (Fig. 1e), indicating stronger ion–dipole interactions and a thermodynamically favored interfacial migration pathway. This strengthened interaction provides a molecular driving force for rapid interfacial Li$^+$ transport and contributes to uniform ion flux distribution during cycling.

The ion-transport properties obtained from experimental characterization corroborate the theoretical predictions. The PP@LATSP@DNA (PPLD) separator was fabricated through

a facile, scalable process compatible with industrial production, yielding a uniform ∼2 µm LATSP@DNA coating on the PP substrate (Fig. S2 and S3). XPS analysis confirms the successful grafting of DNA—evidenced by O–C=O, C–F, and –NO$_2$ signals—demonstrating effective molecular modification of the LATSP surface (Fig. S4). As shown in Fig. 1f (detailed values are listed in Table S1), the pristine PP and PP@LATSP (PPL) separators exhibit ionic conductivities of 0.308 and 0.359 mS cm^{-1}, respectively, whereas PPLD reaches 0.517 mS cm^{-1} with an elevated t_{Li^+} of 0.646 (vs. 0.371 for PP and 0.415 for PPL). To decouple bulk transport in ceramic electrolytes, PP@Al$_2$O$_3$ (PPA) separator was examined. Although PPA shows lower conductivity (0.243 mS cm^{-1}), PP@Al$_2$O$_3$@DNA (PPAD) separator increases this value to 0.411 mS cm^{-1}, confirming that DNA universally enhances Li$^+$ transport at ceramic/liquid electrolyte interfaces. In contrast, PP@LATSP@BA (PPLB) separator delivers only 0.227 mS cm^{-1}, a t_{Li^+} of 0.297, and a Li$^+$ conductivity of 0.067 mS cm^{-1}, highlighting the superiority of the high-dipole DNA molecule. Among all samples, PPLD achieves the highest Li$^+$ conductivity of 0.334 mS cm^{-1}, highlighting its strong ion–dipole interaction capability and superior interfacial regulation efficacy. EIS measurements were conducted on SS‖SS symmetric cells using PPL and PPLD separators from 30 °C to 70 °C, and the activation energy (E_a) was calculated from the Arrhenius plots (Fig. 1g and Table S2). The PPLD separator delivers a lower activation energy (0.09 eV) than PPL (0.14 eV), indicating a reduced barrier for Li$^+$ migration and faster interfacial transport kinetics.

Overall, these theoretical and experimental results jointly demonstrate that the incorporation of DNA establishes a dipole-mediated, partial-solvation environment at the LATSP interface. This interfacial regulation lowers the Li$^+$ migration barrier, strengthens Li$^+$ solvation on LATSP, and accelerates surface ion conduction, collectively enabling fast, uniform, and energetically favorable Li$^+$ transport, which is crucial for stable Li metal operation.

2.2 Chemical stability against the lithium metal anode

LUMO and HOMO energy levels of different solvents and Li salts were calculated using DFT. Fig. 2a shows that the DNA molecule has a significantly lower LUMO energy level (−4.29 eV) compared to the solvents and Li salts in the conventional ether-based electrolyte. This suggests that DNA is probably preferentially reduced on contact with the Li metal, where the –F and –NO$_2$ groups may react with Li to in situ form a Li inorganic component-rich (LiF/Li$_3$N/Li$_2$O) SEI.[34]

To evaluate the enhanced interfacial stability between the LATSP and Li metal through DNA modification, Li‖Li symmetric cells with PPL and PPLD separators were assembled, and their electrochemical impedance spectrum (EIS) were recorded after resting for several days. As shown in Fig. 2b, the interfacial impedance of the PPLD cell increases from 36.2 ohms (day 1) to 40.6 ohms (day 7), with an increment of only 12.15%. In contrast, the impedance of the PPL cell increases from 45.3 ohms (day 1) to 67.5 ohms (day 7), with an increment of 49.0%. This demonstrates that DNA modification effectively
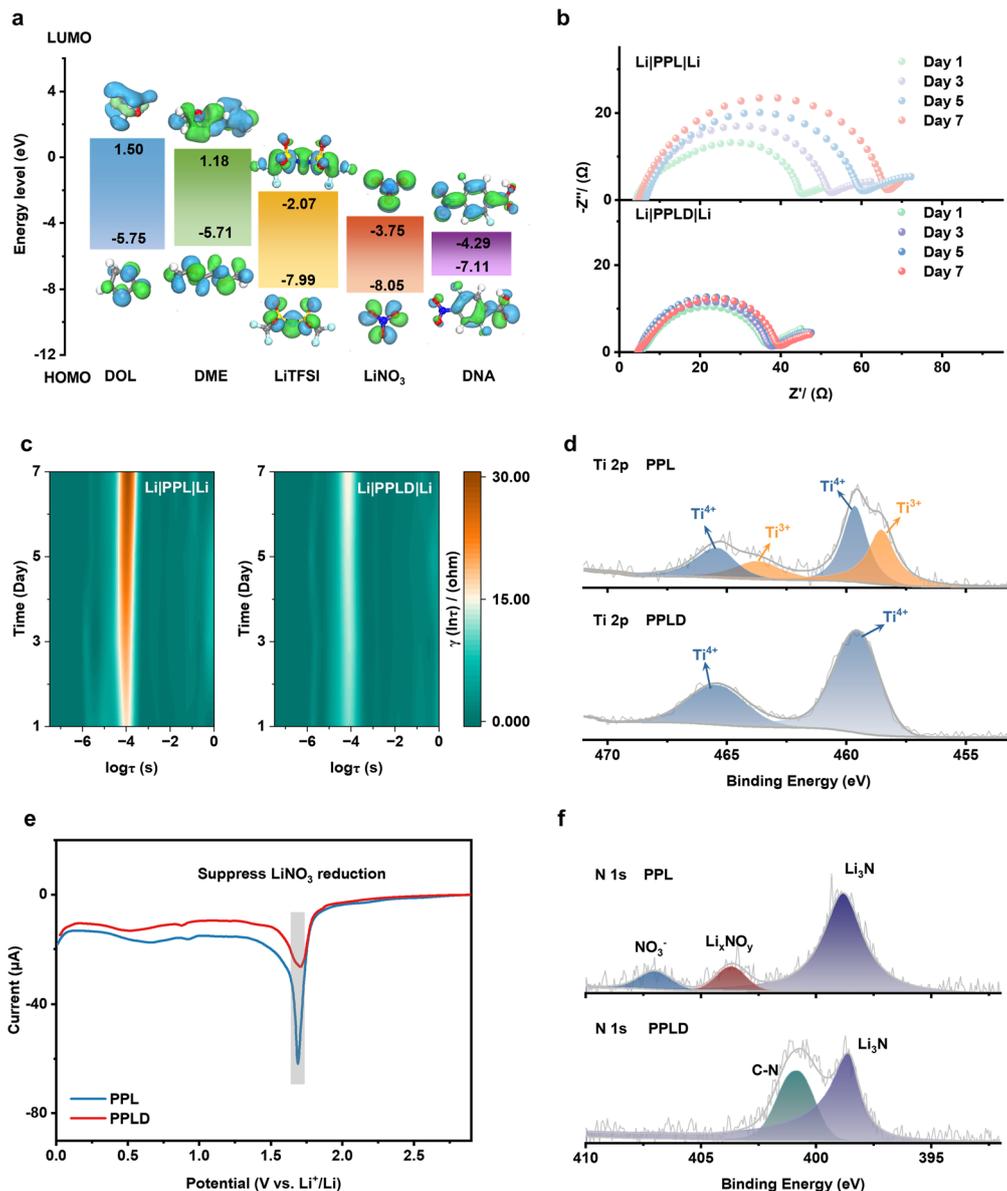
Fig. 2 (a) LUMO and HOMO energy levels of different solvents and Li salts. (b) Nyquist plots of Li‖Li symmetric cells with PPL and PPLD separators at different resting times. (c) DRT analysis of symmetric cells with PPL and PPLD separators at different resting times. (d) Detailed XPS fitting profiles of the Ti valence variation in the LATSP of PPL and PPLD separators in the symmetric cells after a 7-day rest. (e) LSV scanning results of Li/Cu half-cells assembled with PPL and PPLD separators. (f) Detailed XPS spectra N 1s of the Li surface after 7-day rest in a Li‖Li symmetric cell with PPL and PPLD separators.

prevents direct contact between LATSP and Li metal, thereby suppressing the reduction of LATSP by Li metal.

Distribution of relaxation times (DRT) analysis was employed to further elucidate the temporal evolution of interfacial processes (Fig. 2c). The peak observed at $\approx 10^{-4}$ s in the DRT spectra corresponds to the interfacial impedance. For the Li/PPLD/Li symmetric cell, this peak maintains a stable frequency position and relatively low intensity throughout the resting period. In contrast, the Li/PPL/Li symmetric cell exhibits a gradually increasing peak intensity accompanied by a shift of the peak frequency toward lower values. The frequency downshift indicates sluggish reaction kinetics, while the increased

peak intensity reflects hindered ion transport leading to a higher overpotential.[35] Furthermore, XPS testing on the two separators after resting for 7 days reveals that the Ti element in the LATSP of the unmodified separator is partially reduced from Ti^{4+} to Ti^{3+} (Fig. 2d).[25] However, for the DNA-modified separator, the Ti element in the LATSP remains stable in its Ti^{4+} state. These results further confirm that the DNA molecular layer incorporation in stabilizing the LATSP/Li interface.

Next, a typical Li‖Cu half-cell was assembled to analyze the reduction process through linear sweep voltammetry (LSV) testing (Fig. 2e). The reduction peak for $LiNO_3$ appears at approximately 1.7 V.[36] Compared to the PPL-based cell, the

PPLD-based cell exhibits a lower intensity of the $LiNO_3$ reduction peak. Given that the cell was rested for one day before testing, this result implies that the DNA molecules may undergo decomposition during the resting period, thereby pre-forming the SEI and thus reducing the consumption of electrolyte during the electrochemical SEI formation process. Furthermore, XPS was utilized to confirm the chemical composition of the Li surface. After a 7-day rest, the Li surface from the Li‖Li symmetric cell with the PPL separator is characterized with an abundance of NO_3^- and Li_xNO_y, which can be attributed to the decomposition of the electrolyte (Fig. 2f). In contrast, NO_3^- and Li_xNO_y components are not detected on the Li surface of the Li‖Li symmetric cell with the PPLD separator. Meanwhile, the LiF component is more abundant than cell with PPL separator (Fig. S5). These results demonstrate that the protection of LATSP originates from a synergistic mechanism: at the initial contact stage, DNA molecules grafted onto the LATSP surface form a molecular-scale interfacial layer, thereby mitigating the premature reductive decomposition of LATSP. Meanwhile, owing to the low LUMO level of DNA, these molecules undergo preferential reduction on the Li metal surface, leading to the formation of an inorganic-rich SEI layer. This SEI is electronically insulating yet ionically conductive, which effectively blocks further electron transfer while allowing efficient Li^+ transport. The synergistic effects of early-stage molecular passivation and subsequent SEI formation together account for the enhanced chemical stability and transport kinetics observed at the LATSP/electrolyte interface. Fig. S6 presents a schematic diagram illustrating the significant impact of the DNA layer on the interfacial stability between the LATSP and Li metal. The inorganic-rich interphase governs the subsequent interfacial ion transport behavior even if the original organic dipole species are partially consumed, especially those located at or near the Li interface. Moreover, the dipole interaction acts at the LATSP/liquid electrolyte interface and does not involve SEI formation, exerting a continuous effect and improving the Li^+ transport efficiency.

2.3 Electrochemical properties of PPLD separator

To characterize the effect of the DNA layer on Li deposition and stripping behaviors, Li‖Li symmetric cells with PPL and PPLD separators were assembled and analyzed for electrochemical kinetics. As shown in Fig. S7, cyclic voltammetry (CV) tests were performed on different separators to investigate their reaction kinetics further. Compared to the PPL-based cell, the PPLD-based cell exhibits a more distinct current response at the same scan rate, indicating faster Li^+ transport kinetics. In Fig. 3a, the Tafel plot reveals that the exchange current density of the PPLD-based cell increases to 0.255 mA cm^{-2}, compared to 0.102 mA cm^{-2} for the PPL-based cell, further demonstrating the enhanced charge transfer kinetics of the PPLD-based cell.[37]

The Li distribution and deposition behavior on the Cu electrode were studied based on Li‖Cu half-cells. The voltage profile under constant current (Fig. 3b) shows that the PPL separator exhibits a nucleation overpotential of 89 mV, while the PPLD separator demonstrates a lower nucleation

overpotential of 44 mV, indicating a reduced nucleation energy barrier of elemental Li in the presence of DNA. The effect of the PPLD separator on the reversibility of Li deposition was studied by measuring the coulombic efficiency (CE) of the Li‖Cu half-cells, as exhibited in Fig. 3c. The cell using PPLD separator maintains a stable average CE of approximately 98.5% after 150 cycles at a current density of 1.0 mA cm^{-2} and an areal capacity of 1.0 mAh cm^{-2}. In contrast, the CE of the PPL-based cell fluctuates significantly after 50 cycles. The deposition-stripping voltage profiles in Fig. S8 also demonstrate the improved reversibility with the PPLD separator. After 50 cycles at a current density of 1.0 mA cm^{-2} and an areal capacity of 1.0 mAh cm^{-2}, the Li surface morphology on PPL/Cu and PPLD/Cu electrodes was characterized by SEM (Fig. S9). The Li deposited on the PPL/Cu electrode shows a porous, loosely packed, and uneven surface, while the Li deposited on the PPLD/Cu electrode presents a compact and uniform surface.

To further investigate the Li plating/stripping performance, constant current cycling measurements were performed on Li‖Li symmetric cells using PPL and PPLD separators. Fig. S10 shows the Li plating/stripping behavior at a current density of 1.0 mA cm^{-2} and an areal capacity of 1.0 mAh cm^{-2}. Both the PPL-based and PPLD-based cells initially exhibit smooth voltage profiles. However, the PPL-based cell experiences a significant overpotential increase and failure within 200 hours. In contrast, the PPLD-based cell exhibits stable cycling over 1000 hours, demonstrating that the DNA molecular layer effectively stabilizes the Li plating/stripping behavior and extends the lifespan of the Li metal anode.[38]

The morphology of the Li electrodes from symmetric cells after repeated plating/stripping for 50 cycles was characterized by SEM. As shown in Fig. 3d and e, at a high current density of 3 mA cm^{-2} (1 mAh cm^{-2}), the Li electrode cycled with the PPL separator exhibits a rough, porous surface and a loose, mossy cross-sectional morphology, which becomes even more pronounced compared to the lower-current case (Fig. S11). In contrast, the PPLD-based cell delivers a smooth, compact Li surface and a dense deposition structure (Fig. S12), demonstrating that the DNA interfacial layer effectively regulates uniform Li nucleation and growth, particularly under high-rate conditions. DRT analysis provides insight into the interfacial kinetics of the Li electrodes. As shown in Fig. 3f, the PPL-based cell exhibits broader and lower-intensity peaks extending to longer relaxation times, reflecting slower interfacial Li^+ migration processes. In contrast, the PPLD-based cell (Fig. 3g) shows a single dominant peak at short relaxation times with a narrower and higher intensity, indicating fast and uniform Li^+ transport across the interface and a more homogeneous SEI formation. The comparison directly demonstrates that DNA modification not only lowers the interfacial resistance but also accelerates interfacial ion transport, corroborating the EIS and activation energy analyses presented above.

To investigate the effect of the DNA molecular layer on the components and spatial distribution of SEI, time-of-flight secondary ion mass spectrometry (TOF-SIMS) was performed on the Li electrodes of PPL-based and PPLD-based cells after 10 cycles at a current density of 1.0 mA cm^{-2} and an areal capacity
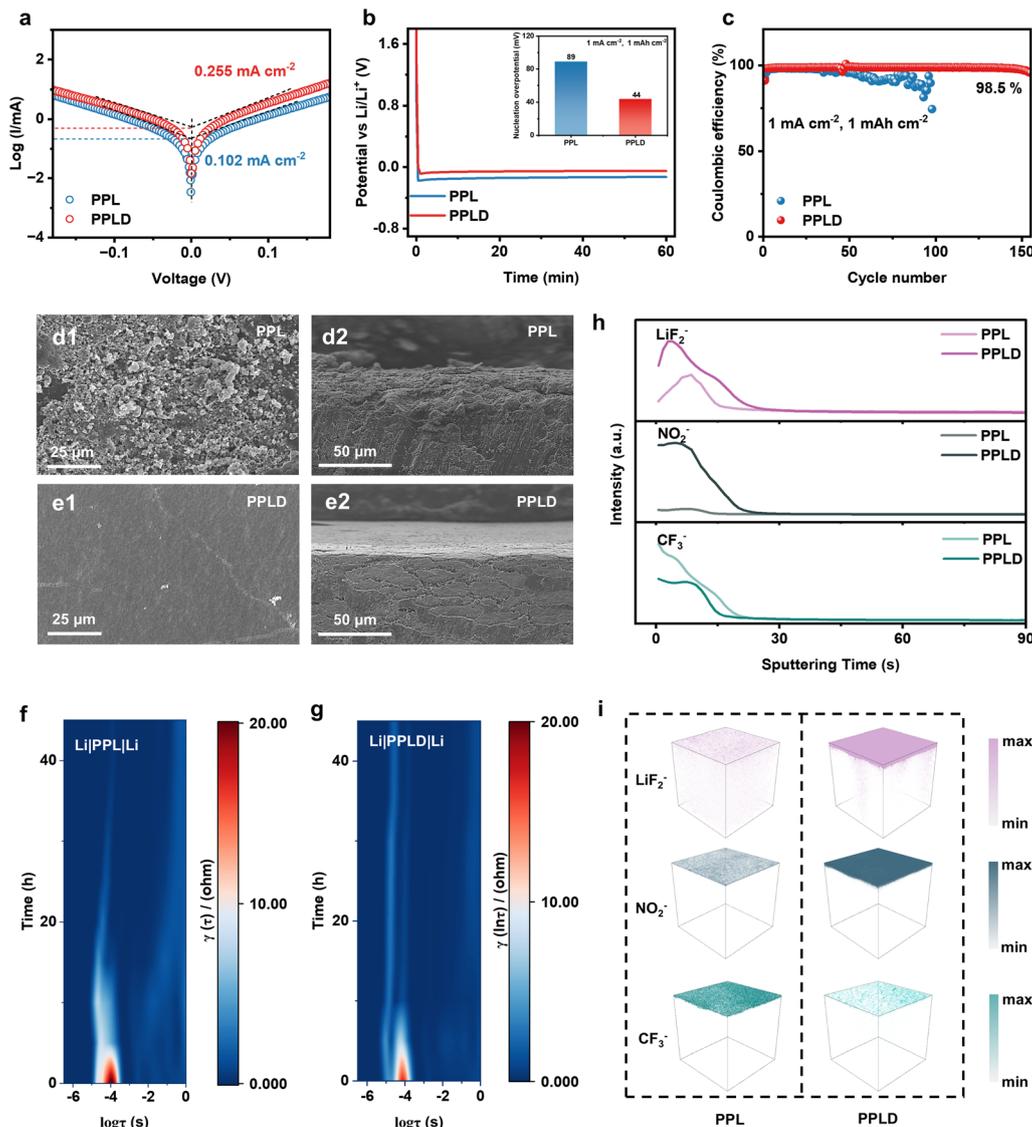
Fig. 3 (a) Tafel curves for symmetrical Li∥Li cells and the corresponding exchange current densities of PPL and PPLD separators. (b) Galvanostatic voltage profiles and corresponding nucleation of Li deposition on Cu electrodes with PPL and PPLD separators at a fixed current density of 1 mA cm^{-2} for 1 h. (c) The cycling coulombic efficiency of Li∥Cu cells with PPL and PPLD separators at a constant current density of 1 mA cm^{-2} and areal capacity of 1 mAh cm^{-2}. SEM images of the Li-metal surface cross section for symmetrical Li∥Li cells with (d1 and d2) PPL and (e1 and e2) PPLD separators after cycling at a constant current density of 3 mA cm^{-2} and areal capacity of 1 mAh cm^{-2}. DRT analyses of Li∥Li symmetric cells with (f) PPL and (g) PPLD separators at current densities of 1 mA cm^{-2}, with an areal capacity of 1 mAh cm^{-2}. (h) TOF-SIMS depth profiles and corresponding 3D visualization of typical secondary ions (LiF$_2^-$, NO$_2^-$, and CF$_3^-$) on the Li electrodes in symmetrical Li∥Li cells after 10 cycles with (i) PPL and PPLD separators.

of 1.0 mAh cm^{-2}. Fig. 3h shows the in-depth profiles of typical secondary-ion signals. Compared to the PP@LATSP separator, the PPLD separator results in more LiF$_2^-$ and NO$_2^-$ in the SEI. This indicates the formation of a more robust inorganic SEI enriched with fluorinated/nitrated species. It should be emphasized that all compared systems employ the same electrolyte formulation containing 2 wt% LiNO$_3$, indicating an additional nitrogen-containing source (the prior reduction of DNA molecules) beyond the electrolyte additive. Notably, the CF$_3^-$ content, which is a signature product of TFSI$^-$ reduction, shows significantly lower intensity in the Li electrode with PPLD

separator. This variation further proves that the DNA molecular layer effectively suppresses the continuous decomposition of the Li salt in the electrolyte. Fig. 3i provides 3D visualizations of the spatial distribution of inorganic SEI components at the interface, in which the LiF$_2^-$ and NO$_2^-$ ions are more densely and uniformly distributed in the SEI with the PPLD separator. These results suggest that the PPLD separator synergistically optimizes SEI composition and Li deposition kinetics, leading to long-life stable cycling of the Li metal anode. These results suggest that interfacial solvation reconfiguration and lowers the interfacial migration barrier, while enabling preferential

interfacial reduction to form a compact LiF/Li_3N-rich interphase.[39–41] This dipole-mediated interfacial solvation regulation homogenizes Li^+ flux and stabilizes Li deposition and offers a promising strategy for dendrite-free Li metal batteries with long-term cycling stability.

2.4 Full-cell performance based on PPLD separators

To further evaluate the practical performance of the PPLD separator, full cells were assembled with $LiFePO_4$ (LFP) and $LiNi_{0.8}Mn_{0.1}Co_{0.1}O_2$ (NMC811) cathodes, respectively. The long-term cycling performance of the Li∥LFP full cells operated at 1C, featuring a LFP mass loading of 7.5 mg cm^{-2} (96.5% active material), is presented in Fig. 4a. Full cells with PPLD separator sustained stable operation for 800 cycles, achieving a consistent CE of approximately 99.9%. Notably, the full cell with PPLD separator maintained 80.26% capacity retention after 700 cycles, whereas the full cell with PPL separator suffered from rapid capacity degradation after 100 cycles, retaining just 78.06% of its initial capacity after 130 cycles. This demonstrates

the crucial role of the DNA molecular layer in ensuring the electrochemical cycling stability of the full cell. The corresponding voltage profiles are shown in Fig. S13, where the PPLD-based cell exhibits less polarization compared to the PPL-based cell. Fig. S14 compares the dQ_m/dv curves of PPL and PPLD-based cells, where the full cell with PPLD separator shows significantly lower shifts in the oxidation-reduction peaks and peak intensity attenuation, indicating effectively suppressed interfacial side reactions, leading to a boosted Li metal anode cycling reversibility.

With the increased LFP mass loading (16 mg cm^{-2}), the full cell with PPLD separator manifested stable operation for 500 cycles, maintaining 85.04% capacity retention and a high and stable CE of approximately 99.95%. In contrast, the discharge capacity of the full cell using PPL separator experienced rapid capacity fading after 100 cycles (Fig. 4b). Fig. 4c displays the discharge rate performance of the full cells with a high LFP mass loading of 16 mg cm^{-2}. The discharge capacities of the Li∥LFP cell with PPL separator are distinctly higher than those of the PP and PPL separator, delivering 172.84, 173.54, 167.82,
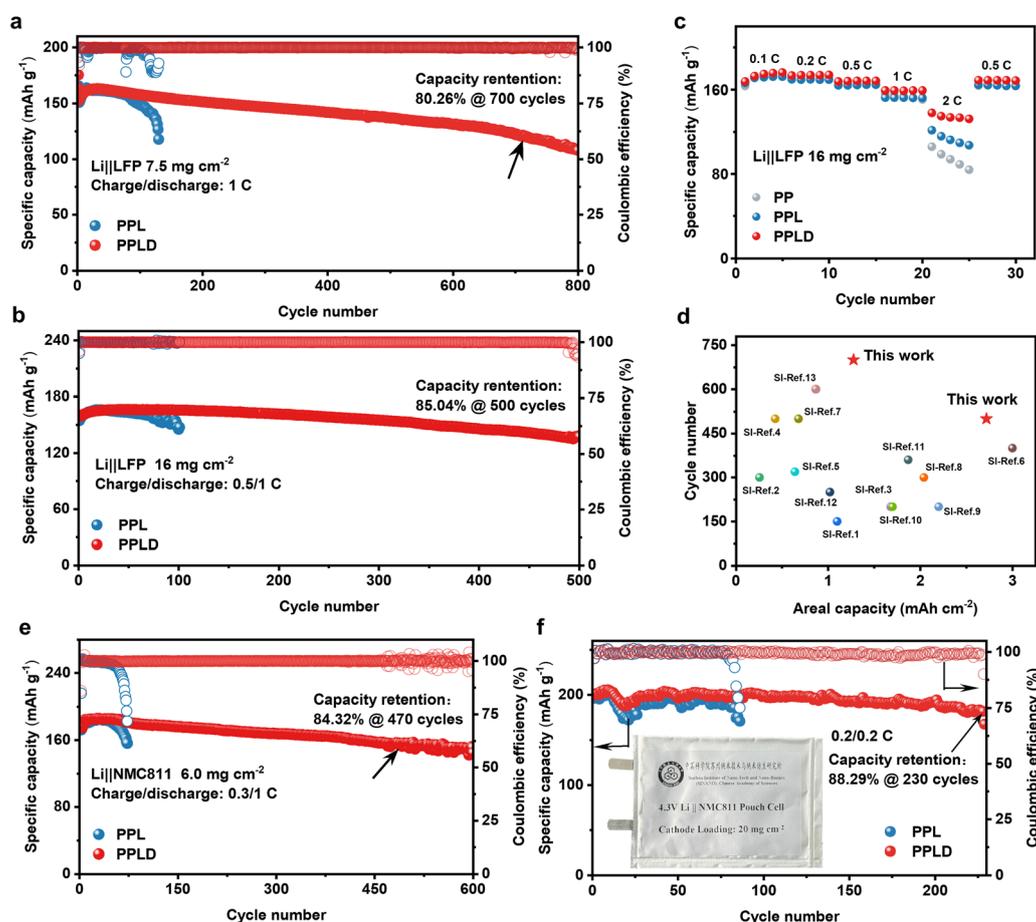

Fig. 4 (a) The cycling performance of Li∥LFP full cells with PPL and PPLD separators using the 7.5 mg cm^{-2} mass loading cathode. (b) Cycling performance of Li∥LFP full cells with PPL and PPLD separators using the 16 mg cm^{-2} mass loading cathode. (c) The rate performance of Li∥LFP cells with PPL and PPLD separators at current densities from 0.1C to 2C, respectively. (d) Comparison of the cycling performance of Li∥LFP batteries between the PPLD separator and other reported modified separators. (e) Cycling performance of Li∥NMC811 full cells with PPL and PPLD separator using the 6.0 mg cm^{-2} mass loading cathode. (f) Cycling performance of the Li∥NMC811 pouch cell at 0.2C with PPL and PPLD separators using a high mass loading cathode of 20 mg cm^{-2}. Inset: the corresponding optical image of the pouch cell.

158.96, and 134.99 mAh g^{-1} at 0.1, 0.2, 0.5, 1, and 2C, respectively, demonstrating that the PPLD separator design boosts the rate capability of LMBs. Compared to other reported separators, the Li‖LFP cell with the PP@LATSP@DNA separator showed notable advantages in terms of cathode areal capacity and long cycle life, significantly enhancing overall performance (Fig. 4d and Table S3).

To further investigate the Li metal anode interfacial chemistry in the full cell, the XPS spectra were collected from the Li metal anode surfaces of PPL-based and PPLD-based cells after cycling and surface cleaning. As shown in Fig. S15 and S16, the SEI formed in the PPLD-based cells after cycling contained significantly more LiF and Li$_3$N components than PPL-based cells. LiF is considered an effective SEI component to suppress Li dendrite growth for its ultra-high mechanical strength and Young's modulus. Meanwhile, the highly Li$^+$ conductive Li$_3$N component mitigates uneven Li$^+$ flux and regulates Li deposition inhomogeneity. Comprehensively, this LiF and Li$_3$N-rich SEI ensures a stable interface with fast Li$^+$ transport and mechanical strength.[42]

Additionally, the long cycling performance of Li‖NMC811 full cell operated at 1C, with an NMC811 loading of 6.0 mg cm^{-2} (96.5% active material), is depicted in Fig. 4e and S17. The discharge capacity of PPLD-based cell decreases from 184.23 mAh g^{-1} to 163.42 mAh g^{-1}, retaining 84.32% of its initial capacity after 470 cycles and exhibiting smaller polarization voltage. In contrast, the PPL-based cell exhibited greater polarization, with discharge capacity decreasing from 182.86 mAh g^{-1} to 156.26 mAh g^{-1} after only 70 cycles. This excellent cycling performance can be attributed to the efficient Li plating/stripping kinetics as well as the well-maintained electrochemical stability introduced by the DNA molecular layer. Fig. S18 shows the rate performance of the Li‖NMC811 full cell. The discharge capacities of the PPLD based cell are significantly higher than those of the PPL based cell, delivering 213.61, 204.05, 197.86, 187.22, 170.28, 141.78, 117.82, and 61.42 mAh g^{-1} at 0.1, 0.2, 0.3, 0.5, 1, 2, 3, and 5C, respectively. The cycling stability and corresponding charge–discharge voltage profiles of the Li‖NMC811 pouch cell are shown in Fig. 4f and S19, respectively. Li‖NMC811 pouch cell with the PPLD separator maintains an 88.29% capacity retention even after 230 cycles at 0.2C, demonstrating the excellent performance of the PPLD separator under near-practical conditions. In summary, the full cell cycling performance highlights the great potential of the PPLD separator in improving the cycling stability of LMBs.

3   Conclusion

In summary, we have developed a dipole-mediated interfacial solvation strategy for the PPLD separator that markedly enhances the performance of LMBs. DFT calculations and electrochemical characterizations reveal that the strong molecular dipole of DNA reorganizes the local Li$^+$ solvation structure and establishes accelerated migration pathways at the separator/electrolyte interface. Besides, DNA molecules are preferentially reduced on the Li metal surface to form a Li$_3$N/LiF-enriched SEI, effectively suppressing excessive electrolyte

decomposition and stabilizing the Li interface. The PPLD separator exhibits high ionic conductivity of 0.517 mS cm^{-1} and a high Li$^+$ transference number of 0.646 at 30 °C, enabling efficient ion transport. Consequently, Li‖LiFePO$_4$ full cells achieve stable cycling over 700 cycles at 1C with 80.26% capacity retention, while Li‖NMC811 full cells maintain 84.32% capacity over 470 cycles at 1C. Even at high cathode loadings (LFP 16 mg cm^{-2}, NMC811 20 mg cm^{-2}), the cells maintain uniform Li deposition and long-term cycling stability. This work demonstrates a dual-interface regulation mechanism of dipole-facilitated interfacial ion transport and *in situ* formation of stable SEI, providing a promising avenue for realizing practical high-energy-density and dendrite-free LMBs.

Author contributions

Conflicts of interest

The authors declare no competing financial interest.

Data availability

The data supporting this article have been included as part of the supplementary information (SI). Supplementary information: further experimental details and additional data/results. See DOI: https://doi.org/10.1039/d5sc09822j.

Acknowledgements

References

1 B. Jagger and M. Pasta, *Joule*, 2023, **7**, 2228–2244.
2 Z. Wu, R. Li, S. Zhang, L. Lv, T. Deng, H. Zhang, R. Zhang, J. Liu, S. Ding, L. Fan, L. Chen and X. Fan, *Chem*, 2023, **9**, 650–664.

3 J. Y. Gan, Y. Zhao, Z. Jiang, C. Y. Yang, D. Ke, Q. C. Wang, Y. Liu, X. H. Zeng and T. F. Zhou, *Chem. Sci.*, 2025, **16**, 18791–18798.

4 G. Lu, J. Nai, D. Luan, X. Tao and X. W. Lou, *Sci. Adv.*, 2023, **9**, eadf1550.

5 X. Cai, S. Zou, Y. Zhao, C. Ma, P. Shi, H. Yuan, J. Luo, Y. Wang, J. Nai, X. Tao and Y. Liu, *Adv. Mater.*, 2025, 2508557.

6 H. Park, Y. Jeon, M. Park, I. Jung, J. Shin, Y. Kim, W. K. Kim, K. H. Ryu, W. B. Lee and J. Park, *ACS Nano*, 2024, **18**, 12885–12896.

7 Q.-K. Zhang, S.-Y. Sun, M.-Y. Zhou, L.-P. Hou, J.-L. Liang, S.-J. Yang, B.-Q. Li, X.-Q. Zhang and J.-Q. Huang, *Angew. Chem., Int. Ed.*, 2023, **62**, e202306889.

8 J. Zhou, B. Hao, M. Peng, L. Zhang, H. Ji, J. Liu, W. Ling, C. Yan and T. Qian, *Adv. Energy Mater.*, 2023, **13**, 2204174.

9 X. Wang, H. Huang, H. Zhang, Q. Dong, W. Zhang, M. Gao, J. Li, B. Chen, H. Guo and X. Han, *Small*, 2024, **20**, 2401100.

10 Y. Luo, S. Z. Huang, J. H. Liao, Z. B. Wu and L. B. Chen, *Chem. Sci.*, 2025, **16**, 9366–9374.

11 J. Sun, F. Kang, D. Yan, T. Ding, Y. Wang, X. Zhou and Q. Zhang, *Angew. Chem., Int. Ed.*, 2024, **63**, e202406511.

12 Y. Cheng, Z. Wang, J. Chen, Y. Chen, X. Ke, D. Wu, Q. Zhang, Y. Zhu, X. Yang, M. Gu, Z. Guo and Z. Shi, *Angew. Chem., Int. Ed.*, 2023, **62**, e202305723.

13 J. Sun, S. Zhang, J. Li, B. Xie, J. Ma, S. Dong and G. Cui, *Adv. Mater.*, 2023, **35**, 2209404.

14 T. Naren, G.-C. Kuang, R. Jiang, P. Qing, H. Yang, J. Lin, Y. Chen, W. Wei, X. Ji and L. Chen, *Angew. Chem., Int. Ed.*, 2023, **62**, e202305287.

15 J. Zhu, D. Cai, J. Li, X. Wang, X. Xia, C. Gu and J. Tu, *Energy Storage Mater.*, 2022, **49**, 546–554.

16 J. Seo, J. Im, M. Kim, D. Song, S. Yoon and K. Y. Cho, *Small*, 2024, **20**, 2312132.

17 S. Su, X. Y. Zhou, W. Z. Liang, Z. R. Su, Y. B. Qu, Y. H. Zhong, J. H. Qiu and B. Zhang, *Chem. Sci.*, 2025, **16**, 19792–19805.

18 X. Zhang, Y. Wu, B. Yu, K. Hu, P. Zhang, F. Ding, L. Zhang, Y. Chen, J. Z. Ou and Z. Zhang, *EcoEnergy*, 2024, **2**, 549–598.

19 Y. Ji, C. Yang, J. Han and W. He, *Adv. Energy Mater.*, 2024, **14**, 2402329.

20 T. Yang, X. Xu, S. Chen, Y. Yang, F. Li, W. Fan, Y. Wu, J. Zhao, J. Liu and Y. Huo, *Angew Chem. Int. Ed. Engl.*, 2025, **64**, e202420973.

21 K. Wang, T. Zhao, R. Lv, W. Tang, T. Yu, L. Li, F. Wu and R. Chen, *Adv. Funct. Mater.*, 2025, e08164.

22 Z. Fan, X. Chen, J. Shi, H. Nie, X. Zhang, X. Zhou, X. Xie and Z. Xue, *Nano-Micro Lett.*, 2025, **17**, 128.

23 W. Zhao, H. Wang, Q. Dong, H. Shao, Y. Zhang, Y. Tang, Y. Shen and L. Chen, *Chem. Eng. J.*, 2025, **505**, 159662.

24 X. Jiang, X. Zhu, X. Ai, H. Yang and Y. Cao, *Appl. Mater. Interfaces*, 2017, **9**, 25970–25975.

25 C. Wang, Y. He, P. Zou, Q. He, J. Li and H. L. Xin, *J. Am. Chem. Soc.*, 2025, **147**, 19084–19092.

26 A. Paolella, X. Liu, A. Daali, W. Xu, I. Hwang, S. Savoie, G. Girard, A. G. Nita, A. Perea, H. Demers, W. Zhu, A. Guerfi, A. Vijh, G. Bertoni, G. C. Gazzadi, G. Berti, C. Sun, Y. Ren, K. Zaghib, M. Armand, C. Kim, G.-L. Xu and K. Amine, *Adv. Funct. Mater.*, 2021, **31**, 2102765.

27 Y. Wang, X. Chang, Z. Li, Y. Mei, Y. Zhang, L. Liu, K. Wang, H. Gu and L. Li, *Adv. Funct. Mater.*, 2023, **33**, 2208329.

28 Z. Li, S. Zhou, X. Wu, B. Zhang, X. Yu, F. Pei, H.-G. Liao, Y. Qiao, H. Zhou and S.-G. Sun, *Adv. Funct. Mater.*, 2023, **33**, 2211774.

29 M. Zhang, K. Liu, Y. Gan, H. Wang, F. Liu, M. Bai, X. Tang, Z. Wang, S. Li, A. Shao, K. Zhou, T. Wang, Z. Wang, S. Yuan and Y. Ma, *Adv. Energy Mater.*, 2022, **12**, 2201390.

30 L. Ding, X. Yue, Y. Chen, Z. Wang, J. Liu, Z. Shi and Z. Liang, *Adv. Funct. Mater.*, 2023, **33**, 2304386.

31 R. Yi, Y. Mao, Y. Shen and L. Chen, *J. Am. Chem. Soc.*, 2021, **143**, 12897–12912.

32 S. Lv, X. He, Z. Ji, S. Yang, L. Feng, X. Fu, W. Yang and Y. Wang, *Adv. Energy Mater.*, 2023, **13**, 2302711.

33 S. Lv, G. Wen, W. Cai, S. Yang, J. Yang, Y. Zhai, X. Fu, W. Yang and Y. Wang, *J. Energy Chem.*, 2025, **103**, 48–58.

34 J. Pokharel, A. Cresce, B. Pant, M. Y. Yang, A. Gurung, W. He, A. Baniya, B. S. Lamsal, Z. Yang, S. Gent, X. Xian, Y. Cao, W. A. Goddard III, K. Xu and Y. Zhou, *Nat. Commun.*, 2024, **15**, 3085.

35 T. Zhang, X. Zhu, J. Xiong, Z. Xue, Y. Cao, K. C. Gordon, G. Xu and M. Zhu, *Nat. Commun.*, 2025, **16**, 4867.

36 C. Ma, Q. Qiao, K. Yue, J. Yue, X. Cai, J. Zheng, L. Kang, Y. Wang, J. Nai, J. Luo, H. Yuan, S. Zou, X. Tao and Y. Liu, *Adv. Funct. Mater.*, 2024, **34**, 2406479.

37 J. Chen, X. Deng, X. Jia, Y. Gao, H. Chen, Z. Lin and S. Ding, *J. Am. Chem. Soc.*, 2024, **146**, 30836–30847.

38 X.-X. Luo, S.-J. Tan, J. Zhang, J.-C. Guo, C.-H. Zhang, Y.-H. Wang, W.-L. Wang, J.-S. Wu, X.-L. Wu and Y.-G. Guo, *Angew. Chem., Int. Ed.*, 2025, **64**, e202500135.

39 C. Wang, K. Wan, P. Liu, C. Zeng, S. Wang, Y. Huang, Y. Zhang, H. Xiao, C. Shu and Z. Liang, *Angew. Chem., Int. Ed.*, 2025, **64**, e202506083.

40 C. Wang, T. Ouyang, X. Wang, S. Liu, G. Tian, F. Fan, P. Liu, S. Wang, C. Zeng and C. Shu, *J. Energy Chem.*, 2024, **99**, 384–392.

41 P. Liu, C. Wang, C. Zeng, S. Wang, X. Yu, H. Xiao, Y. Huang, Y. Zhang, Y. Zeng, C. Shu and Z. Liang, *SusMat*, 2025, **5**, e70007.

42 Y. Hu, W. Zhang, J. Shi, Y. Li, H. Cheng, D. Li, F. Li, H. Wang, D. Cheng, K. Huang, Z. Li, Y. Wei, H. Xu and Y. Huang, *ACS Nano*, 2024, **18**, 33418–33429.